

Magnetoconductance, Quantum Hall Effect, and Coulomb Blockade in Topological Insulator Nanocones

Raphael Kozlovsky, Ansgar Graf, Denis Kochan, Klaus Richter, Cosimo Gorini^{1,*}

¹*Institut für Theoretische Physik, Universität Regensburg, 93040 Regensburg, Germany*
(Dated: November 16, 2021)

Magnetotransport through cylindrical topological insulator (TI) nanowires is governed by the interplay between quantum confinement and geometric (Aharonov-Bohm and Berry) phases. Here, we argue that the much broader class of TI nanowires with varying radius – for which a *homogeneous* coaxial magnetic field induces a *varying* Aharonov-Bohm flux that gives rise to a non-trivial mass-like potential along the wire – is accessible by studying its simplest member, a TI nanocone. Such nanocones allow to observe intriguing mesoscopic transport phenomena: While the conductance in a perpendicular magnetic field is quantized due to higher-order topological hinge states, it shows resonant transmission through Dirac Landau levels in a coaxial magnetic field. Furthermore, it may act as a quantum magnetic bottle, confining surface Dirac electrons and leading to a largely interaction-dominated regime of Coulomb blockade type. We show numerically that the above-mentioned effects occur for experimentally accessible values of system size and magnetic field, suggesting that TI nanocone junctions may serve as building blocks for Dirac electron optics setups.

Electronic transport across phase-coherent structures has been a central topic of solid state research ever since the birth of mesoscopic physics some 40 years ago. While the complexity of mesoscopic setups has steadily increased, from the simple gate-defined quantum point contacts of the '80s [1] to elaborate present-day electron optics circuits in semiconductors [2] and graphene [3, 4], their structure remains in the vast majority of cases planar – *i.e.* transport takes place in flat two-dimensional (2D) space. Exceptions to the 2D scenario are samples based on carbon nanotubes and 3D topological insulator (3DTI) nanowires [5–8]. 3DTIs are bulk band insulators hosting protected 2D surface metallic states à la Dirac [9]. In mesoscopic nanostructures built out of 3DTIs low-temperature phase-coherent transport takes place on a 2D Dirac metal wrapped around an insulating 3D bulk. As such, it is strongly dependent on a peculiar conjunction of structural (real space) and spectral (reciprocal space) geometrical properties. This has remarkable consequences for a topological insulator nanowire (TINW) with constant circular cross section in a coaxial magnetic field, shown in Fig. 2(a). Its magnetoconductance reflects a non-trivial interplay between two fundamentals of mesoscopic physics: quantum confinement and geometric [Aharonov-Bohm (AB) and Berry] phases [6–8, 10–12].

An interesting twist offered by 3DTIs is the possibility of engineering shaped TINWs with a variable cross section, *e.g.* truncated TI nanocones (TINC) as sketched in Fig. 1(a). When a coaxial magnetic field is switched on, shaped TINWs possess the unique feature that surface charge carriers traversing the wire, experience not only a variation of the centrifugal potential, but also a spatially changing AB flux – a property that cannot easily be realized with bulk conductors. This gives rise to a flux-dependent effective mass potential along the TINC, which induces a variety of interesting mesoscopic transport phenomena, including resonant transport through

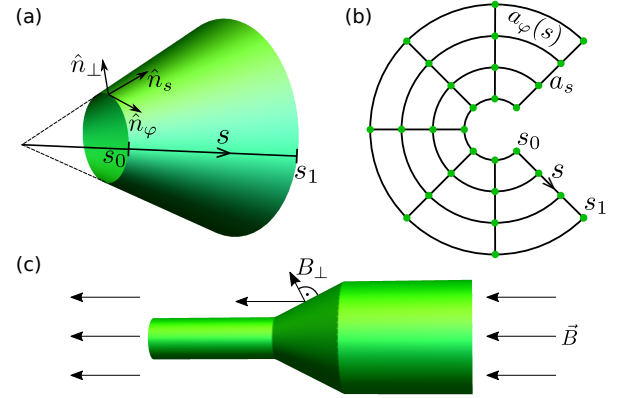


FIG. 1. (a) Sketch of a TINC extended to its conical singularity with local coordinate vectors $\hat{n}_\varphi, \hat{n}_s, \hat{n}_\perp$. (b) Unfolded cone grid used for numerical simulations. (c) TINC in coaxial B-field (with $B_\perp = \vec{B} \cdot \hat{n}_\perp$) with cylindrical leads attached.

Dirac Landau levels and magnetically induced Coulomb blockade physics. Due to the non-trivial real space geometry, all such transport regimes can be accessed simply by applying and tuning a homogeneous magnetic field.

Cylindrical TINW in a magnetic field – For later reference consider cylindrical TINWs of radius R in coaxial [6–8, 10–12] or perpendicular [13–20] magnetic fields. They can be described by the 2D surface Dirac Hamiltonian [21] $H = v_F [\frac{1}{2} (p_\varphi \sigma_\varphi + \sigma_\varphi p_\varphi) + \sigma_z p_z]$ with Fermi velocity v_F , coordinate along the wire axis z , and azimuthal angle φ . Furthermore, $p_\varphi = \frac{-i\hbar}{R} \partial_\varphi$ and $\sigma_\varphi = \sigma_y \cos \varphi - \sigma_x \sin \varphi$ with Pauli matrices $\sigma_x, \sigma_y, \sigma_z$. The unitary transformation $U = \exp(i\sigma_z \varphi/2)$ yields $H = v_F (\sigma_y p_\varphi + \sigma_z p_z)$ and antiperiodic boundary conditions for the wave functions. The associated Berry phase [22] shifts the angular momentum quantization condition by $\hbar/2$, yielding a gapped subband spectrum $E_l(p_z) = \pm v_F \sqrt{p_z^2 + \hbar^2(l + 1/2)^2/R^2}$, with orbital angu-

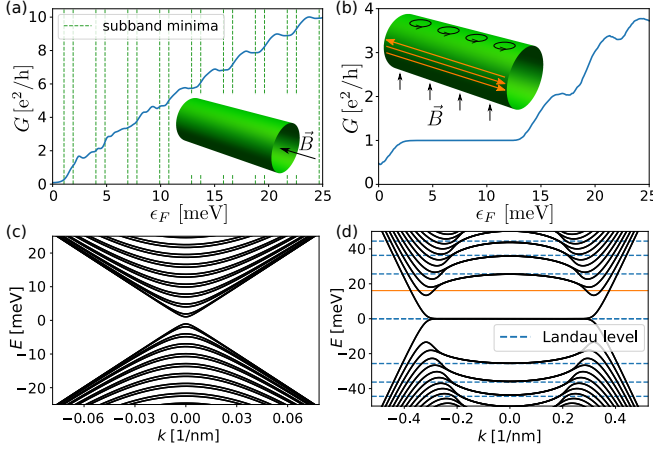


FIG. 2. Disorder-averaged conductance as function of the Fermi energy ϵ_F (top panels) and band structure (with longitudinal wave number k , bottom) of a cylindrical TI nanowire in a coaxial (left) and perpendicular (right) magnetic field $B = 2$ T. The orange arrows in (b) sketch 1D hinge states at an energy marked with an orange line in (d). Wire size: length $L = 600$ nm, circumference $C = 700$ nm. We use a Gaussian-correlated disorder average taken over 600 configurations, and a Fermi velocity of $v_F = 5 \times 10^5$ m/s here and throughout.

lar momentum quantum number $l \in \mathbb{Z}$. For a coaxial B -field generating a magnetic flux $\Phi = \pi R^2 B$ ($B = |\mathbf{B}|$) through the tube the problem remains separable and reduces to that of an electron in an AB ring – the cylinder cross section – times free longitudinal motion. The discrete spectrum of the ring is periodic in Φ_0 [23], and is turned into a series of 1D subbands by free longitudinal motion. Due to the Berry phase the bands are gapped for $\Phi = n\Phi_0$ and gapless for $\Phi = (n + 1/2)\Phi_0$, $n \in \mathbb{Z}$ [10, 11]. Figure 2(c) shows the generic situation with $\Phi \approx 18.86\Phi_0$. The corresponding conductance is depicted in Fig. 2(a), increasing with energy as more channels open [8]. For details of the numerics see below and the Supp. Mat. [24].

If the magnetic field is orthogonal to the nanowire axis, the situation changes drastically. The resulting band structure, see Fig. 2(d), can be understood qualitatively in classical terms [25]: The field component $B_\perp = B \cos \varphi$ perpendicular to the surface varies along the wire circumference, being maximal for $\varphi = 0, \pi$ (cylinder top and bottom) and zero for $\varphi = \pi/2, 3\pi/2$ (sides), where its sign changes. Cyclotron orbits [black circles in Fig. 2(b)] of opposite handedness thus form on the top and bottom surfaces, while “snaking” orbits propagating along the sides appear (orange arrows). Quantum mechanically, the former lead to Landau level (LL) formation, while the latter are chiral 1D hinge states crossing the B_\perp -induced gap and signaling a higher-order TI phase [26]. The dashed lines in Fig. 2(d) mark the LL energies

for $B = B_\perp$ ($\varphi = 0$),

$$E_n = \text{sgn}(n) \frac{\hbar v_F}{l_B} \sqrt{2|n|}, \quad n \in \mathbb{Z}, \quad (1)$$

where $l_B = \sqrt{\hbar/(eB)}$ is the magnetic length. Around $k=0$, flat bands represent well-formed LLs. The upward (downward) bending $n=0$ subband ensures the existence of a robust conductance plateau $G = e^2/h$ in a large energy window, see Fig. 2(b), where only one chiral hinge state per side is present, preventing backscattering. The dip at $\epsilon_F = 0$ is treated in Ref. [20].

TINC in a coaxial magnetic field – We generalize our considerations to a TINC, see Fig. 1(a), a representative building block of TINWs with varying cross section. We parametrize its surface by the azimuthal angle φ and the distance s to the conical singularity. The radius is $R(s) = s \sin(\beta/2)$, β denoting the cone opening angle and $s_0 \leq s \leq s_1$. Using standard techniques [48] and after the unitary transformation $U = \exp(i\sigma_z \varphi/2)$, the surface Dirac Hamiltonian reads

$$H = v_F \left[\left(p_s - \frac{i\hbar}{2s} \right) \sigma_z + p_\varphi(s) \sigma_y \right], \quad (2)$$

with $p_\varphi(s) = -\frac{i\hbar}{R(s)} \partial_\varphi$. The spin connection term $-\frac{i\hbar}{2s}$ [27] makes it Hermitian with respect to the scalar product

$$\langle \Psi_1 | \Psi_2 \rangle \equiv \int_{s_0}^{s_1} ds \int_0^{2\pi} d\varphi R(s) \Psi_1^*(s, \varphi) \Psi_2(s, \varphi). \quad (3)$$

Transforming $\Psi \rightarrow \tilde{\Psi} = \sqrt{R(s)} \Psi$ and $H \rightarrow \tilde{H} = \sqrt{R(s)} H (1/\sqrt{R(s)})$ removes the spin connection term from Eq. (2) and renders the volume form $R(s) d\varphi ds$ trivial. This yields

$$\tilde{H} = v_F [p_s \sigma_z + p_\varphi(s) \sigma_y], \quad (4)$$

with $\langle \tilde{\Psi}_1 | \tilde{\Psi}_2 \rangle \equiv \int ds \int d\varphi \tilde{\Psi}_1^*(s, \varphi) \tilde{\Psi}_2(s, \varphi)$, which is necessary for our numerics [24].

In presence of a coaxial magnetic field the problem remains rotationally symmetric and thus separable. We proceed via the *exact* separation ansatz $\tilde{\Psi}_{nl}(s, \varphi) = e^{i(l+1/2)\varphi} \chi_{nl}(s)$, with $\chi_{nl}(s)$ a two-component spinor. The $+1/2$ in the exponential originates from the curvature-induced Berry phase, l is the orbital angular momentum quantum number, and the meaning of n will be clarified shortly. Using minimal coupling $p_\varphi(s) \rightarrow p_\varphi(s) + eA_\varphi(s)$ yields the 1D Dirac equation

$$[v_F p_s \sigma_z + V_l(s, B) \sigma_y] \chi_{nl}(s) = \epsilon_{nl} \chi_{nl}(s). \quad (5)$$

Here, the angular momentum term

$$V_l(s, B) = \frac{v_F \hbar}{R(s)} \left(l + \frac{1}{2} - \frac{\Phi(s, B)}{\Phi_0} \right), \quad (6)$$

with $\Phi(s, B) = \pi R^2(s) B$, acts as a position-dependent mass potential, and is crucial for predicting the TINC

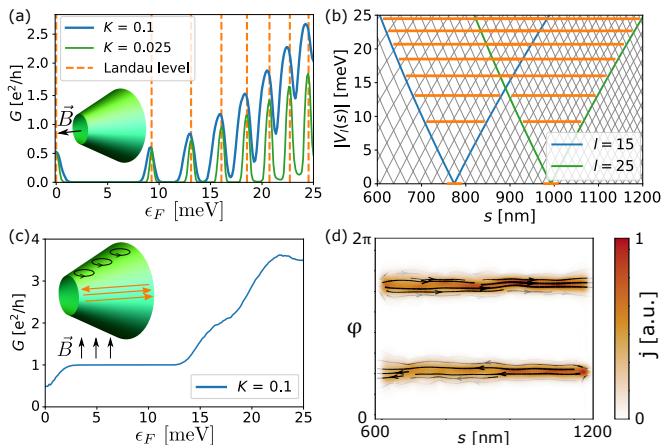


FIG. 3. Disorder averaged TI nanocone conductance for coaxial and perpendicular magnetic field. (a) Coaxial field: resonant transmission through LLs. Stronger disorder (larger K [24]) broadens and shifts the LLs from their unperturbed positions marked by vertical dashed lines [31, 32]. (b) LL formation in effective wedge potentials. (c) Perpendicular field: robust conductance plateau due to topologically protected chiral hinge states and associated current density in (d). Parameters: $B = 2$ T; cone with (arc) length 600 nm and opening angle $\beta = 15^\circ$, beginning a distance $s_0 = 600$ nm away from the conical singularity, yielding minimal and maximal circumferences $C_{\min} \approx 492$ nm, $C_{\max} \approx 984$ nm (see Fig. 1).

magnetotransport properties – indeed, more generally the properties of arbitrarily shaped, rotationally symmetric TINWs [28]. Its mass-like character becomes evident in Eq. (5), where it couples to σ_y , while a simple electrostatic potential enters the equation with the identity matrix. Hence, Eq. (5) describes 1D Dirac electrons feeling the *effective potential* $|V_l(s)|$. Dirac electrons Klein-tunnel through electrostatic barriers, but not through $|V_l(s)|$. Figure 3(b) shows $|V_l(s, B)|$ for a coaxial B -field, whose B_\perp yields $l_B \ll s_1 - s_0$ for all l -values relevant in the presented energy range (only $l = 15$ and $l = 25$ are colored and labeled, the rest is gray). In transport, an electron injected in mode l feels a distinct effective potential $|V_l(s, B)|$. For a discussion of the B -field dependence of $|V_l(s, B)|$ and the formation of wedges shown in Fig. 3(b) see [24]. Note that due to the step-like form of $B_\perp(s)$, cf. Fig. 1(c), the situation is similar to single-valley graphene subject to a magnetic barrier [29, 30].

Magnetotransport through TINCs – Our quantum transport simulations including disorder are based on the software package *kwant* [33]. The tight-binding representation of Eq. (2) is non-Hermitian due to the non-trivial volume form [24]. The latter is rendered trivial by the transformation $H \rightarrow \tilde{H}$, hence Eq. (4) has a Hermitian tight-binding representation. Conventional discretization of Eq. (4) leads to the effective lattice shown in Fig. 1(b), representing the unfolded cone. The transversal lattice constant $a_\varphi(s)$, which is part of the hopping integral,

is adapted such that $N_\varphi a_\varphi(s) = U(s)$, where N_φ is the number of lattice points and $U(s)$ the circumference at position s , and the ends are “glued” together (for details see [24]). To compute the conductance, highly-doped semi-infinite cylindrical leads with radii $R(s_0)$ and $R(s_1)$ are attached to the conical scattering region, see Fig. 1(c).

Figure 3(a) shows the TINC conductance for the potential $|V_l(s, B)|$ in Fig. 3(b). Sharp peaks signal resonant transmission through quasi-bound states of wedge-shaped effective potentials: Each wedge (labeled by l) hosts a sequence of bound states (labeled by n) whose energies $\{\epsilon_{nl}\}$, marked by horizontal orange lines in Fig. 3(b), are solutions of Eq. (5). The latter are quantum Hall (QH) states, degenerate in l and forming the Dirac LL given in Eq. (1). The LL degeneracy is thus given by the number of wedges within the cone (between s_0 and s_1). In a clean TINC degenerate states in adjacent wedges are orthogonal, hence transport is exponentially suppressed. Disorder breaks rotational symmetry and couples adjacent states leading to broadened resonant tunneling peaks, see Fig. 3(a). Indeed, stronger disorder increases the coupling between QH states, and thus the conductance (compare green and blue curves). Note the close relation to a QH Corbino geometry [34]: Looking at the TINC from the front, its 2D projection is a ring of finite thickness in a homogeneous perpendicular magnetic field B_\perp .

For a TINC in a B -field orthogonal to its symmetry axis, the conductance is completely different, see Fig. 3(c). Its main features – dip at zero energy, plateau up to $E \simeq 13$ meV and subsequent disorder-smoothed steps – stem from second-order topological hinge states at the sides. If $l_B \ll \pi R(s_0)$, they are indistinguishable from those of a cylindrical TINW, cf. Figs. 2(b) and 3(c). This is actually true in a much more general sense: As long as top and bottom surface provide enough space for LLs to form, the geometry of the TINW in perpendicular B -field is irrelevant for the qualitative conductance features, as opposed to TINWs in coaxial B -field. The current density associated with the lowest-energy hinge state of the TINC, yielding the robust plateau, is plotted in Fig. 3(d) and seen to be chiral – the current on opposite sides ($\varphi = \pi/2, 3\pi/2$) flows in opposite directions.

The two settings in Fig. 3(a) and (c) correspond to a longitudinal (σ_{xx}) and transversal (σ_{xy}) conductivity measurement in a conventional 2D QH setup where the longitudinal current density reads $j_x = \sigma_{xx}E_x + \sigma_{xy}E_y$. Let us adapt this to the TINC. In a perpendicular magnetic field, E_x vanishes as long as ϵ_F lies within the plateau due to lack of backscattering. Hence, the conductance is solely determined by σ_{xy} . On the contrary, in a coaxial magnetic field E_y vanishes since metallic states extend across the circumference, resulting in a conductance determined by σ_{xx} only.

Coulomb blockade in smoothed TINCs – Equation (5)

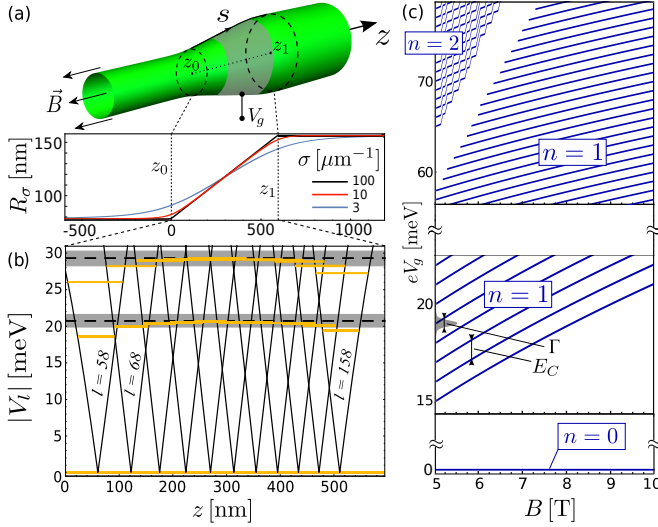


FIG. 4. Anomalous Coulomb blockade in TI nanocones. (a) Smoothed TINC parametrized by $R_\sigma(z)$ [24] with $\sigma = 10 \mu\text{m}^{-1}$ (small σ corresponds to strong smoothing, see lower panel). A gate wrapping around the TINC is sketched by the gray region. (b) $|V_l(z)|$ from $l = 58$ to $l = 158$ (in steps of $\Delta l = 10$) are shown for $B = 10$ T. QH states (marked by orange lines) with $n \neq 0$ are no longer resonant across the entire junction, leading to tunnel barriers close to z_0, z_1 . Grey shade depicts the disorder broadening Γ from Fig. 3(a) for $K = 0.1$. (c) Addition spectrum of the $n = 0, 1, 2$ LLs in the central TINC region, with charging energy $E_C = 1$ meV. The $n = 1, 2$ LLs, defined by QH states whose energy lies within the disorder broadening, are Coulomb split by E_C , while $n = 0$ QH states are not affected by Coulomb repulsion.

and thus the concept of an effective potential, Eq. (6), is valid more generally for any rotationally symmetric but arbitrarily shaped TINWs, the coordinate s generalizing to an arc length coordinate [28]. Exploiting the effective potential, one can devise different wire geometries featuring (tunable) magnetic barriers able to confine Dirac electrons [28]. As a simple and paradigmatic example, we consider a smoother, more realistically shaped TINC, see Fig. 4(a). In the regions of smaller slope (close to the leads) B_\perp decreases to zero, ergo the QH states drop in energy and are no longer resonant with those in the center: a QH island representing a quantum magnetic bottle emerges in the central TINC region between magnetic tunnel barriers close to the leads.

To confirm the above qualitative statements numerically, we consider the setup of Fig. 4(a). For convenience we work with the coaxial coordinate z instead of s . The radius $R_\sigma(z)$ is now characterized by a smoothing parameter σ introducing surface curvature, $d^2 R_\sigma / dz^2 \neq 0$. The ideal TINC from Fig. 3 is recovered for $\sigma \rightarrow \infty$ [24], see Fig. 4(a). Orange lines in Fig. 4(b) mark the bound state energies of the potential wedges $|V_l(z)|$, obtained by solving the generalized version of Eq. (5). QH states with $n > 0$ close to the leads are strongly low-

ered in energy as compared to the central ones, which still form the (disorder-broadened) LLs expected in the limit $\sigma \rightarrow \infty$. Effective magnetic confinement requires the smooth TINC border region to be larger than the (local) magnetic length l_B , so that off-resonant QH states can form, corresponding to B -field strengths of order 5–10 T for the smooth TINC considered. Larger TINCs or smoother border regions allow for weaker magnetic fields. Notably, the $n = 0$ LL is unaffected by the magnetic flux modulation, a distinct feature of Dirac electrons. This leads to an anomalous coexistence of transport mechanisms: $n = 0$ electrons stay delocalized and the associated conductance resonant, while potential barriers close to z_0, z_1 confine $n \neq 0$ electrons, whose transport properties are then dominated by Coulomb repulsion. Indeed, when the Fermi energy aligns with an $n \neq 0$ LL, oscillations of Coulomb blockade type [35] should be observed by varying the gate voltage V_g applied to the central TINC region.

An exact description of blockade oscillations in strong magnetic fields is a highly non-trivial many-body problem that, in the case of semiconductors, is often solved self-consistently [36]. However, the general features of the addition spectrum can usually be obtained from the constant interaction model, characterized by a constant charging energy E_C , and the single-particle spectrum of the island [36]. Hence, we stay within such a model and discuss the expected consequences. Figure 4(c) shows the addition spectrum of the inner LLs as function of B assuming homogeneous gating and $E_C = 1$ meV (this value is justified below). The $n = 0$ LL is open to the leads and thus not split by interaction effects. Conductance peaks belonging to the $n = 1$ LL are constantly spaced in gate voltage. The large gap in the upper panel is the Landau gap between the first and second LLs. For increasing B , additional QH states join the $n = 1$ LL, adding to its degeneracy and shifting upwards the bottom of the $n = 2$ LL in steps of E_C . If the coupling $\Gamma_n^{l,r}$ to the left (l) and right (r) leads is roughly the same for all QH states within the n -th LL, one expects conductance peaks $G_n \propto \Gamma_n^l \Gamma_n^r / (\Gamma_n^l + \Gamma_n^r)$ [35]. Besides the anomalous $n = 0$ conductance peak, further differences between standard Coulomb blockade [36] and the present scenario are evident: First, the blockade conductance is determined by the Dirac spectrum $\propto \sqrt{B}$, not the one $\propto B$ of trivial electrons; Second, the island-lead coupling – and thus the conductance peaks height and shape – is determined by the tunable magnetic barrier $\Gamma_n^{l,r}(B)$. Its precise characterization is a non-trivial, setup-dependent problem. Finally, the $n \neq 0$ islands are neither featureless resonant levels as in the simple quantum dots, nor do they host QH edge states running along their perimeter [36]. In fact, transport across each island is akin to that through a peculiar disordered system whose transmission increases with increasing disorder [see Fig. 3(b)]. Thus, our setting might host a competition between magnetically-induced

blockade physics and a suitable generalization of (longitudinal) magnetotransport physics for 2D, disordered systems [37, 38], which is unexplored ground. Its study appears as a very interesting problem, albeit clearly beyond the scope of this work.

Experimental realization – The parameters used are within experimental reach: HgTe-based 3DTI tubes [8] or core-shell nanowires [39] with spatially varying cross sections have already been built for transport experiments. Crucially, our conclusions do not require the TINC to have a truly circular cross section: Surface deformations lift the degeneracies of the QH states within each LL, but as long as this splitting is smaller than the broadening due to, *e.g.* temperature or disorder, no qualitative conductance change is expected. Moreover, the leads are not required to have a cylindrical shape. To achieve our results, it is merely important that there are enough lead modes available that couple to the states on the TINC. The charging energy E_C depends on the setup size, geometry and materials, including the dielectrics, and can thus be tuned in a broad range. For a HgTe-based TINC with parameters from Ref. [8], E_C is of the order of 1 meV. Homogeneous gating can be achieved with established techniques [40, 41].

Conclusions – Shaped TINWs represent a broad class of mesoscopic junctions realizable with current technology which allow to explore radically different magnetotransport regimes. The latter result from the interplay between magnetic confinement of Dirac electrons, disorder and interactions. They are all accessible in TINCs by tuning a homogeneous magnetic field, and orienting it in space. TINCs and junctions thereof could act as building blocks of more complex 3D mesoscopic Dirac electron setups, where, *e.g.*, exotic aspects of QH physics on curved surfaces can be studied [44, 45], or of TI-superconducting systems where Majoranas are looked for [9, 42, 43].

Acknowledgements – We thank Andrea Donarini, Benjamin Geiger, Milena Grifoni, Dmitry Polyakov, and Alex Kamenev for useful discussions. This work was funded by the Deutsche Forschungsgemeinschaft (DFG, German Research Foundation) – Project-ID 314695032 – SFB 1277 (project A07 and B07), and within Priority Programme SPP 1666 “Topological Insulators” (project Ri681-12/2). Support by the Elitenetzwerk Bayern Doktorandenkolleg “Topological Insulators” is also acknowledged.

* cosimo.gorini@physik.uni-regensburg.de

- [1] B. J. van Wees, H. van Houten, C. W. J. Beenakker, J. G. Williamson, L. P. Kouwenhoven, D. van der Marel, and C. T. Foxon, “Quantized conductance of point contacts in a two-dimensional electron gas,” *Phys. Rev. Lett.* **60**, 848–850 (1988).
- [2] E. Bocquillon, V. Freulon, F. D. Parmentier, J.-M. Berroir, B. Plaçais, C. Wahl, J. Rech, T. Jonckheere, T. Martin, C. Grenier, D. Ferraro, P. Degiovanni, and G. Fève, “Electron quantum optics in ballistic chiral conductors,” *Ann. Phys. (Berlin)* **526**, 1 (2013).
- [3] N. Kumada, F. D. Parmentier, H. Hibino, D. C. Glatli, and P. Roulleau, “Shot noise generated by graphene p-n junctions in the quantum Hall effect regime,” *Nat. Commun.* **6**, 8068 (2015).
- [4] P. Makk, C. Handschin, E. Tóvári, K. Watanabe, T. Taniguchi, K. Richter, M.-H. Liu, and C. Schönenberger, “Coexistence of classical snake states and Aharonov-Bohm oscillations along graphene p - n junctions,” *Phys. Rev. B* **98**, 035413 (2018).
- [5] H. Peng, K. Lai, D. Kong, S. Meister, Y. Chen, X.-L. Qi, S.-C. Zhang, Z.-X. Shen, and Y. Cui, “Aharonov-Bohm interference in topological insulator nanoribbons,” *Nat. Mater.* **9**, 225 (2009).
- [6] J. Dufouleur, L. Veyrat, A. Teichgräber, S. Neuhaus, C. Nowka, S. Hampel, J. Cayssol, J. Schumann, B. Eichler, O. G. Schmidt, B. Büchner, and R. Giraud, “Quasiballistic Transport of Dirac Fermions in a Bi₂Se₃ Nanowire,” *Phys. Rev. Lett.* **110**, 186806 (2013).
- [7] S. Cho, B. Dellabetta, R. Zhong, J. Schneeloch, T. Liu, G. Gu, M. J. Gilbert, and N. Mason, “Aharonov-Bohm oscillations in a quasi-ballistic three-dimensional topological insulator nanowire,” *Nat. Commun.* **6**, 7634 (2015).
- [8] J. Ziegler, R. Kozlovsky, C. Gorini, M.-H. Liu, S. Weishäupl, H. Maier, R. Fischer, D. A. Kozlov, Z. D. Kvon, N. Mikhailov, S. A. Dvoretzky, K. Richter, and D. Weiss, “Probing spin helical surface states in topological HgTe nanowires,” *Phys. Rev. B* **97**, 035157 (2018).
- [9] M. Z. Hasan and C. L. Kane, “Topological Insulators,” *Rev. Mod. Phys.* **82**, 3045 (2010).
- [10] P. M. Ostrovsky, I. V. Gornyi, and A. D. Mirlin, “Interaction-Induced Criticality in \mathbb{Z}_2 Topological Insulators,” *Phys. Rev. Lett.* **105**, 036803 (2010).
- [11] J. H. Bardarson, P. W. Brouwer, and J. E. Moore, “Aharonov-Bohm Oscillations in Disordered Topological Insulator Nanowires,” *Phys. Rev. Lett.* **105**, 156803 (2010).
- [12] J. Dufouleur, E. Xypakis, B. Büchner, R. Giraud, and J. H. Bardarson, “Suppression of scattering in quantum confined 2D helical Dirac systems,” *Phys. Rev. B* **97**, 075401 (2018).
- [13] H. Ajiki and T. Ando, “Electronic states of carbon nanotubes,” *J. Phys. Soc. Jpn.* **62**, 1255–1266 (1993).
- [14] O. Vafek, “Quantum hall effect in a singly and doubly connected three-dimensional topological insulator,” *Phys. Rev. B* **84**, 245417 (2011).
- [15] Y.-Y. Zhang, X.-R. Wang, and X. C. Xie, “Three-dimensional topological insulator in a magnetic field: chiral side surface states and quantized Hall conductance,” *J. Phys. Condens. Matter* **24**, 015004 (2012), 1103.3761.
- [16] M. Sitte, A. Rosch, E. Altman, and L. Fritz, “Topological insulators in magnetic fields: quantum Hall effect and edge channels with a nonquantized θ term,” *Phys. Rev. Lett.* **108**, 126807 (2012).
- [17] L. Brey and H. A. Fertig, “Electronic states of wires and slabs of topological insulators: Quantum hall effects and edge transport,” *Phys. Rev. B* **89**, 085305 (2014).
- [18] F. de Juan, R. Ilan, and J. H. Bardarson, “Robust Transport Signatures of Topological Superconductivity in Topological Insulator Nanowires,” *Phys. Rev. Lett.* **113**, 107003 (2014).

- [19] E. J. König, P. M. Ostrovsky, I. V. Protopopov, I. V. Gornyi, I. S. Burmistrov, and A. D. Mirlin, “Half-integer quantum Hall effect of disordered Dirac fermions at a topological insulator surface,” *Phys. Rev. B* **90**, 165435 (2014).
- [20] E. Xypakis and J. H. Bardarson, “Conductance fluctuations and disorder induced $\nu = 0$ quantum Hall plateau in topological insulator nanowires,” *Phys. Rev. B* **95**, 35415 (2017).
- [21] Y. Zhang and A. Vishwanath, “Anomalous Aharonov-Bohm Conductance Oscillations from Topological Insulator Surface States,” *Phys. Rev. Lett.* **105**, 206601 (2010).
- [22] G. P. Mikitik and Yu. V. Sharlai, “Manifestation of Berry’s Phase in Metal Physics,” *Phys. Rev. Lett.* **82**, 2147 (1999).
- [23] U. Eckern and P. Schwab, “Normal persistent currents,” *Adv. Phys.* **44**, 387 (1995).
- [24] See Supplemental material.
- [25] P. Onorato, “Landau levels and edge states in carbon nanotubes: A semiclassical approach,” *Phys. Rev. B* **84**, 233403 (2011).
- [26] See [46]. More precisely, we deal here with a second-order TI phase due to the applied magnetic field, and thus *extrinsic* [16], as opposed to *intrinsic* higher-order phases arising from crystal symmetries [47].
- [27] M. Fecko, “Differential geometry and lie groups for physicists,” Cambridge university press (2006).
- [28] R. Kozlovsky et al., to be published.
- [29] A. De Martino, L. Dell’Anna, and R. Egger, “Magnetic Confinement of Massless Dirac Fermions in Graphene,” *Phys. Rev. Lett.* **98**, 066802 (2007).
- [30] M. Ramezani Masir, P. Vasilopoulos, A. Matulis, and F. M. Peeters, “Direction-dependent tunneling through nanostructured magnetic barriers in graphene,” *Phys. Rev. B* **77**, 235443 (2008).
- [31] N. M. R. Peres, F. Guinea, and A. H. Castro Neto, “Electronic properties of disordered two-dimensional carbon,” *Phys. Rev. B* **73**, 125411 (2006).
- [32] B. Dóra, “Disorder effect on the density of states in Landau quantized graphene,” *Low Temp. Phys.* **34**, 801–804 (2008).
- [33] C. W. Groth, M. Wimmer, A. R. Akhmerov, and X. Waintal, “Kwant: A software package for quantum transport,” *New J. Phys.* **16**, 063065 (2014).
- [34] A. Rycerz, “Magnetoelectricity of the Corbino disk in graphene,” *Phys. Rev. B* **81**, 121404(R) (2010).
- [35] C. W. J. Beenakker, “Theory of Coulomb-blockade oscillations in the conductance of a quantum dot,” *Phys. Rev. B* **44**, 1646–1656 (1991).
- [36] U. Meirav and E. B. Foxman, “Single-electron phenomena in semiconductors,” *Semicond. Sci. Technol.* **11**, 255–284 (1996).
- [37] W. Schirmacher, B. Fuchs, F. Höfling, and T. Franzosch, “Anomalous magnetotransport in disordered structures: Classical edge-state percolation,” *Phys. Rev. Lett.* **115**, 240602 (2015).
- [38] I. A. Dmitriev, A. D. Mirlin, D. G. Polyakov, and M. A. Zudov, “Nonequilibrium phenomena in high Landau levels,” *Rev. Mod. Phys.* **84**, 1709–1763 (2012).
- [39] M. Kessel, J. Hajer, G. Karczewski, C. Schumacher, C. Brüne, H. Bühhmann, and L. W. Molenkamp, “CdTe-HgTe core-shell nanowire growth controlled by RHEED,” *Phys. Rev. Materials* **1**, 023401 (2017).
- [40] K. Storm, G. Nylund, L. Samuelson, and A. P. Micolich, “Realizing Lateral Wrap-Gated Nanowire FETs: Controlling Gate Length with Chemistry Rather than Lithography,” *Nano Lett.* **12**, 1 (2012).
- [41] M. Royo, M. De Luca, R. Rurali, and I. Zardo, “A review on III-V core-multishell nanowires: Growth, properties, and applications,” *J. Phys. D Appl. Phys.* **50**, 143001 (2017).
- [42] A. Cook and M. Franz, “Majorana fermions in a topological-insulator nanowire proximity-coupled to an *s*-wave superconductor,” *Phys. Rev. B* **84**, 201105(R) (2011).
- [43] J. Manousakis, A. Altland, D. Bagrets, R. Egger, and Yoichi Ando, “Majorana qubits in a topological insulator nanoribbon architecture,” *Phys. Rev. B* **95**, 165424 (2017).
- [44] D.-H. Lee, “Surface States of Topological Insulators: The Dirac Fermion in Curved Two-Dimensional Spaces,” *Phys. Rev. Lett.* **103**, 196804 (2009).
- [45] T. Can, Y. H. Chiu, M. Laskin, and P. Wiegmann, “Emergent Conformal Symmetry and Geometric Transport Properties of Quantum Hall States on Singular Surfaces,” *Phys. Rev. Lett.* **117**, 266803 (2016).
- [46] F. Schindler, A. M. Cook, M. G. Vergniory, Z. Wang, S. S. P. Parkin, B. A. Bernevig, and T. Neupert, “Higher-Order Topological Insulators,” *Sci. Adv.* **4** (2018).
- [47] M. Geier, L. Trifunovic, M. Hoskam, and P. W. Brouwer, “Second-order topological insulators and superconductors with an order-two crystalline symmetry,” *Phys. Rev. B* **97**, 205135 (2018).
- [48] E. Xypakis, J.-W. Rhim, J. H. Bardarson, and R. Ilan, “Perfect transmission and Aharonov-Bohm oscillations in topological insulator nanowires with nonuniform cross section,” *Phys. Rev. B* **101**, 045401 (2020).
- [49] L. Susskind, “Lattice fermions,” *Phys. Rev. D* **16**, 3031–3039 (1977).
- [50] R. Stacey, “Eliminating lattice fermion doubling,” *Phys. Rev. D* **26**, 468–472 (1982).
- [51] K. M. Masum Habib, R. N. Sajjad, and A. W. Ghosh, “Modified Dirac Hamiltonian for efficient quantum mechanical simulations of micron sized devices,” *Appl. Phys. Lett.* **108**, 113105 (2016).

Supplemental material to the paper

“Magnetoelectroconductance, Quantum Hall Effect, and Coulomb Blockade in Topological Insulator Nanocones”

Raphael Kozlovsky, Ansgar Graf, Denis Kochan, Klaus Richter, Cosimo Gorini¹

¹*Institut für Theoretische Physik, Universität Regensburg, 93040 Regensburg, Germany*

(Dated: November 16, 2021)

NUMERICAL IMPLEMENTATION

Kwant takes as an input tight-binding Hamiltonians of nanostructures and applies the so-called wave function approach to compute their electronic transport properties using the Landauer-Büttiker formalism [33]. Tight-binding Hamiltonians are passed to *kwant* as “conventional” Hermitian matrices, i.e. finite dimensional matrices which fulfill $(H^*)^T = H$. However, discretizing the continuum Hamiltonian Eq. (2) leads to a tight-binding representation which does not fulfill this condition. Let us clarify that the reason for this is the non-trivial (non-constant, i.e. coordinate dependent) volume form. Consider, for simplicity, a one-dimensional system with real space coordinate q and volume form $dV = g(q)dq$. On the lattice, we use the shorthand notation $g_i \equiv g(q_i)$ as well as $\Psi_i \equiv \Psi(q_i)$, where i labels the lattice sites. The condition for the Hermiticity of H , $\langle \Phi | H \Psi \rangle = \langle H \Phi | \Psi \rangle$, is then given by

$$\sum_{ij} g_i \Phi_i^* H_{ij} \Psi_j = \sum_{ij} g_j (H_{ji} \Phi_i)^* \Psi_j \quad (7)$$

on the lattice. From Eq. 7, it is, in general, only possible to deduce that $(H^*)^T = H$ if $g(q) = \text{const.}$ Hence, we use the local transformation

$$H \rightarrow \tilde{H} = \sqrt{g(q)} H (1/\sqrt{g(q)}), \quad (8)$$

$$\Psi \rightarrow \tilde{\Psi} = \sqrt{g(q)} \Psi \quad (9)$$

which makes the volume form trivial. This can be easily seen by considering the scalar product

$$\langle \Phi | H \Psi \rangle = \int_{-\infty}^{\infty} dq g \Phi^* H \Psi \quad (10)$$

$$= \int_{-\infty}^{\infty} dq (\sqrt{g} \Phi^*) \left(\sqrt{g} H \frac{1}{\sqrt{g}} \right) (\sqrt{g} \Psi) \quad (11)$$

$$= \int_{-\infty}^{\infty} dq \tilde{\Phi}^* \tilde{H} \tilde{\Psi}. \quad (12)$$

Note that in Eq. 12, g is fully absorbed in the wave functions and the Hamiltonian, the volume form is trivial. Hence, using the transformation Eq. 8 yields a tight-binding Hamiltonian \tilde{H} which fulfills $(\tilde{H}^*)^T = \tilde{H}$.

We implement the magnetic fields via usual Peierls phases and consider standard Gaussian-correlated disorder,

der,

$$\langle V(\mathbf{r}) V(\mathbf{r}') \rangle = K \frac{\hbar v_F}{2\pi \xi^2} e^{-|\mathbf{r}-\mathbf{r}'|^2/2\xi^2}, \quad (13)$$

with disorder strength K and correlation length ξ . For our simulations we use $K = 0.1$ and $\xi = 7$ nm. To avoid the fermion doubling problem [49, 50], we use a conventional Wilson mass term. For a recent discussion see Ref. [51]. Note that a Wilson mass affects the specifics of the spin-momentum texture. Such specifics are, however, irrelevant for our charge transport problem.

EFFECTIVE MASS POTENTIAL FOR THE TI NANOCONE IN WEAK COAXIAL MAGNETIC FIELD

In order to develop a feeling of how the effective potential $|V_l(s, B)|$ defined in Eq. (6) affects transport, we consider the conductance through a clean TINC (with the same geometry as in Fig. 3) for zero and weak coaxial magnetic field without doping in the leads.

The conductance for $B = 0$ as a function of the Fermi energy ϵ_F , depicted in Fig. 5 (a), shows equidistant conductance steps of size $2e^2/h$. Their position and height can be explained with the corresponding effective potentials, which are plotted in Fig. 5(b) for all l -values which are relevant in the depicted energy range. The central region in between the black vertical lines ($600 \text{ nm} \leq s \leq 1200 \text{ nm}$) corresponds to the truncated cone, while the regions $s < 600 \text{ nm}$ and $s > 1200 \text{ nm}$ correspond to straight leads. The leads are modeled by semi-infinite cylindrical nanowires, thus $|V_l(s, B)|$ is constant. Note that for $B = 0$, the effective potential $|V_l(s)| \propto |l + 0.5|/R(s)$ is purely determined by the finite size confinement energy, hence the spacing in the left lead (smaller circumference), is larger than in the right lead (larger circumference). Modes which enter the scattering region (the truncated cone) via the leads are described by a well defined orbital angular momentum quantum number l , and each of them feels the effective potential $|V_l(s)|$. As soon as the Fermi energy surpasses the effective potential for a given l , the corresponding mode has enough energy to traverse the TINC and a step in the conductance appears. Since there is no disorder and modes are twofold degenerate in

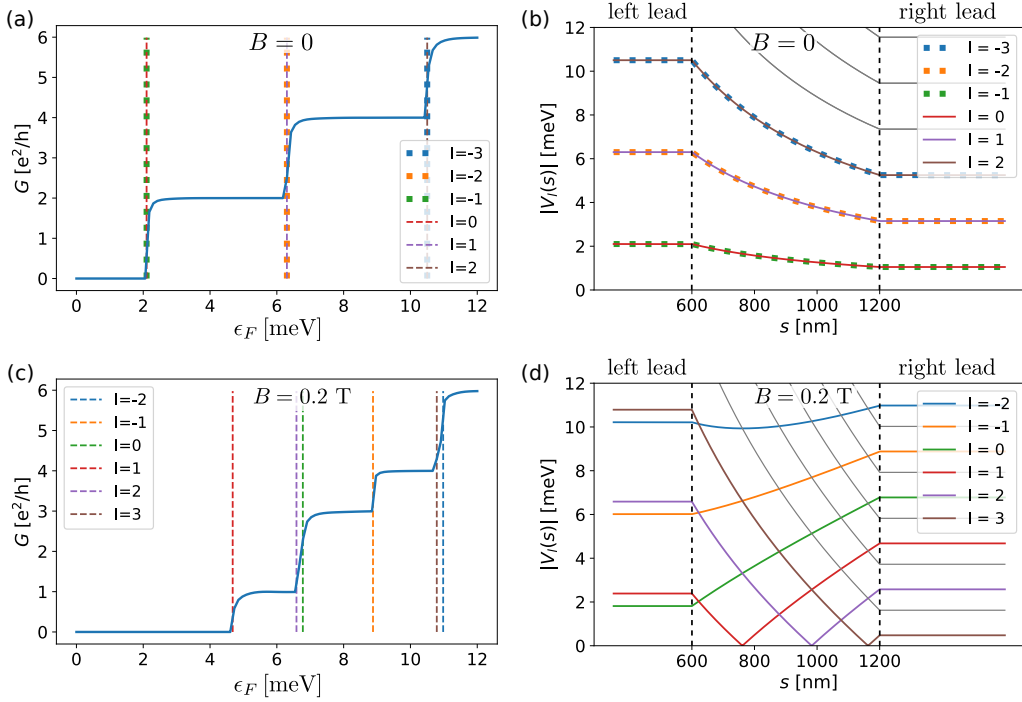


FIG. 5. Conductance as a function of Fermi energy (left panels) and effective potentials (right panels) for a clean TI nanocone with leads, see Fig. 1(c). Panels (a) and (b) correspond to $B = 0$, panels (c) and (d) to a coaxial magnetic field $B = 0.2$ T. Steps in the conductance appear whenever the Fermi energy ϵ_F surpasses one of the effective potentials $|V_l(s, B)|$ labeled by l (corresponding energies are marked by vertical lines). For the conductance simulations we used *kwant* and a Fermi velocity of $v_F = 5 \times 10^5$ m/s.

orbital momentum, the conductance is quantized in units of $2e^2/h$.

In Fig. 5 (c) and Fig. 5 (d), the conductance and the effective potential for a coaxial magnetic field of $B = 0.2$ T is shown. For low energies $\lesssim 2$ meV, the characteristic effective potential “wedges”, ubiquitous in Fig. 3(b) (strong magnetic field $B = 2$ T), start to emerge. In the conductance, a more complicated step sequence appears with step sizes of e^2/h and $2e^2/h$ since orbital angular momentum degeneracy is broken due to the magnetic flux. The first step in the conductance, which is of size e^2/h , appears at ≈ 4.75 meV which corresponds to the opening of the $l = 1$ mode [red curve in (d)]. Modes with $l = 0$ (green curve) and $l = 2$ (purple curve) appear almost at the same energy around 6.75 meV. The proximity of those two mode openings leads to a step size in the conductance of $2e^2/h$.

Note that due to rotational symmetry, modes cannot change their orbital angular momentum quantum number l . However, as soon as rotational symmetry is broken, for instance, by disorder, modes couple. This coupling forms the basis of the resonant transport through Dirac LLs (consisting of bound states of effective poten-

tial wedges) discussed in the main manuscript.

SMOOTHED TI NANOCONE

For the description of a smoothed TINC we choose to work with the coaxial coordinate z . We approximate the Heaviside step function by $\Theta_\sigma(z - z') = \frac{1}{2} + \frac{1}{\pi} \arctan[\sigma(z - z')]$, $\lim_{\sigma \rightarrow \infty} \Theta_\sigma(z - z') = \Theta(z - z')$. The radius of a junction that starts with a cylinder of radius R_0 at $z = -\infty$ and becomes a cylinder of radius R_1 at $z = \infty$ with an intermediate smoothed TINC can then be written as

$$R_\sigma(z) = R_0 + (R_1 - R_0)\Theta_\sigma(z - z_1) + \mathcal{S}(z - z_0)[\Theta_\sigma(z - z_0) - \Theta_\sigma(z - z_1)], \quad (14)$$

where $\mathcal{S} = (R_1 - R_0)/(z_1 - z_0)$ is the slope of a TINC with initial radius R_0 , final radius R_1 and length $z_1 - z_0$. The input parameters chosen for Fig. 4 are such that in the limit $\sigma \mapsto \infty$ the function (14) agrees with the TINC studied in Fig. 3. Thus $R_0 = C_{\min}/(2\pi) = 78.3$ nm, $R_1 = 2R_0 = C_{\max}/(2\pi) \approx 156.6$ nm, $z_0 = 0$ and $z_1 = 594.7$ nm.